

Embedded metal nanopatterns as a general scheme for enhanced broadband light absorption

Fan Ye, Michael J. Burns, and Michael J. Naughton*

Department of Physics, Boston College, 140 Commonwealth Avenue, Chestnut Hill, MA 02467, USA

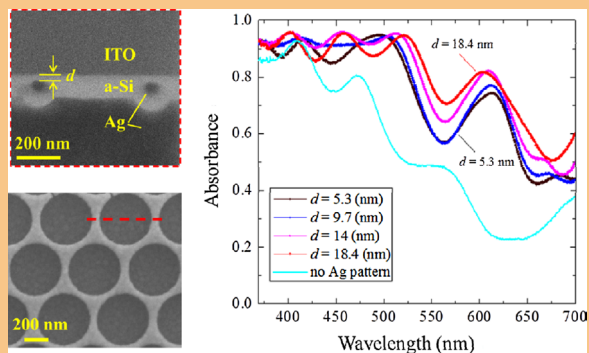
Received 28 July 2014, revised 31 August 2014, accepted 29 September 2014

Published online 24 October 2014

Keywords broadband enhanced absorption, embedded metal nanopattern, metamaterial, optical impedance match, plasmonics

*Corresponding author: e-mail naughton@bc.edu, Phone: +1 617 552 3575, Fax: +1 617 552 8478

Recently, various light trapping schemes based on inclusions of dielectric or metallic nanoparticles or nanopatterns on top of, below, or embedded within a photovoltaic (PV) absorber have been proposed to enhance the efficiency of solar cells. We demonstrate here that embedded metal nanopatterns (EMN) within the absorber layers of thin film solar cells can serve as a general scheme for broadband light absorption enhancement. The EMN scheme is compatible with a wide variety of non-crystalline solar cells, including amorphous, polycrystalline, organic, polymeric, and dye-sensitized solar cells. Simulations on the same EMN in various PV media show consistent absorption enhancement. An impedance matching model is used to explain the robustness of the effect, wherein the EMN brings the impedance of the thin-film solar cell closer to that of free space in a broadband manner, resulting in exceptional absorption enhancement in the near band gap regime. Experimental verifications are provided by Ag connecting network nanopatterns fabricated by nanosphere lithography embedded in an amorphous silicon layer, resulting in a broadband absorbance enhancement, especially in the near band gap region, in good agreement with our predictions.



Connecting Ag networks with hexagonal close-packed holes are fabricated by nanosphere lithography, and then embedded into an amorphous silicon layer. For increasing embedding depth d from 5.3 to 18.4 nm, the absorbance of the structure increases, especially at the near band gap region.

© 2014 WILEY-VCH Verlag GmbH & Co. KGaA, Weinheim

1 Introduction In recent years, various light trapping schemes based on inclusions of metallic nanoparticles or nanopatterns have been proposed to enhance the efficiency of solar cells [1–14]. Such schemes include randomly positioned nanoparticles, and 1D and 2D metallic patterns on top of [1–6], on the bottom of [7, 8], or embedded within [9–14] the photovoltaic (PV) layers. Most of these methods result in modulating one surface of the solar cell, and are thus more compatible with solar cells using thin film PV layers [1–14]. In earlier work, we showed theoretically that there exists an optimum position for the inclusion of a metallic nanopattern in a PV film to achieve maximum absorption within that film [13].

Here, we demonstrate both experimentally and theoretically that the embedded metallic nanopattern (EMN) concept can serve as a general design scheme for enhancing light absorption for a broad range of thin film solar cells, such as amorphous, polycrystalline, organic, and others. We employ an impedance matching model to understand the absorbance enhancement of the EMN scheme over a broad frequency range. We provide experimental measurements on samples with metal nanopatterns embedded in amorphous silicon (a-Si) layers with tuned embedding depths to show the broadband absorption enhancement of the proposed EMN scheme. The EMN scheme may find broad applications in the solar cell industry.

2 Numerical modeling and experimental details

Figure 1a shows the schematic illustration of the simplified structure of an EMN solar cell. In contrast to conventional patterning schemes that employ metal or dielectric patterns or particles on the top [1–6] or the bottom [7, 8] of a PV layer, we have proposed to embed the metal nanopatterns into the absorber layers to fully utilize the near field scattering of the metal patterns for maximized broadband light absorption [13]. Such an EMN scheme is general for various shapes of metal nanopatterns, and is also generic for all kinds of PV media. Two representative metal patterns are shown on the right panel of Fig. 1a: a cross array, and a connecting metal network with hexagonal close-packed (hcp) holes. The cross-pattern is best known for its role in a metamaterial “perfect absorber” that achieves near unity absorption at a certain resonant frequency [15]. As will be shown below, a cross array embedded into an absorber layer with a back reflector can create multiple high absorption peaks and lead to quasi-broadband high absorption. The hcp-hole EMN pattern performs similarly, and in addition can be produced in a scalable way via nanosphere lithography (NSL) [16, 17].

Numerical simulations in this work are full-wave simulations carried out in the radio frequency module of COMSOL MultiPhysics, a commercial software package based on finite element methods. For each simulation, a unit cell of the periodic structure is considered, with boundaries

along the x - and y -axes set to be periodic, thus simulating an infinite sample. An x -polarized plane wave is incident along z into the unit cell on the glass side of the structure. Most of the incident light is absorbed in the PV layer, some is reflected back to the input port, and virtually no light is transmitted through due to the optically thick back reflector. The reflection coefficient is obtained from the scattering parameter S_{11} , and the transmission coefficient from S_{21} . Absorption can be calculated by $A = 1 - |S_{11}|^2 - |S_{21}|^2$.

An impedance matching model is employed to understand the near unity absorption peaks of the EMN patterns [18]. The relative effective impedance $Z_{\text{eff}} = Z_{\text{re}} + iZ_{\text{im}}$ of the unit cell is defined from the extracted effective permittivity ϵ_{eff} and permeability μ_{eff} from the S -parameters, by $Z_{\text{eff}} = (\mu_{\text{eff}}/\epsilon_{\text{eff}})^{1/2}$. The extraction is performed using the method of Smith et al. [19–21], with the reference planes of the two ports set 500 nm away from the sample surface. Denoting the effective thickness of the sample (distance between the two reference planes) as t , and the vacuum wavenumber of the incident wave as k , Z_{eff} can also be directly related to the S -parameters as $Z_{\text{eff}} = \pm [((1 + S_{11})^2 - e^{2ikt} S_{21}^2) / ((1 - S_{11})^2 - e^{2ikt} S_{21}^2)]^{1/2}$, with the signs fixed by the passive material requirement, $Z_{\text{re}} > 0$ [19]. When the relative effective impedance of the unit cell is matched to that of air, i.e., $Z_{\text{re}} = 1$ and $Z_{\text{im}} = 0$, the reflectance of the unit cell is vanishingly small. Combining this result with the fact that the transmission of the unit cell is zero (ensured by the thick back reflector), this leads to near unity absorbance.

Figure 1b and c shows SEM micrographs of a fabricated hcp-hole EMN sample, embedded in an ultrathin (106 nm) a-Si layer. The hcp-hole Ag network was created using NSL [16, 17]. The radii of the original polystyrene (PS) nanospheres were ~ 500 nm, which were then shrunk via reactive ion etching to control the hole size of the subsequent electron beam-evaporated Ag network. The resultant radius after a 60 s etch was $r_s = 227$ nm, yielding a Ag network with a width of ~ 50 nm at its narrowest. The embedded hcp-hole pattern was created in a three-step process: a thin layer of a-Si (h_1) was first deposited onto ITO glass (~ 500 nm of ITO) via PECVD; then an hcp-hole Ag network was defined on the a-Si layer via NSL as described above; finally, a second layer of a-Si with thickness h_2 was deposited onto the whole sample. This was followed by a thick (250 nm) Ag deposition as the back reflector. All of the samples were fabricated such that the total thickness of the a-Si layer ($h = h_1 + h_2 = 106$ nm) is fixed. Thus, by varying h_1 , one can arbitrarily tune the embedding depth ($d = h_1$) of the hcp-hole EMN. The fabricated hcp-hole EMN sample had a total area of ~ 1 cm². The reflectance of the fabricated sample was measured by an integrating sphere reflectometer (Ocean Optics, ISP-REF).

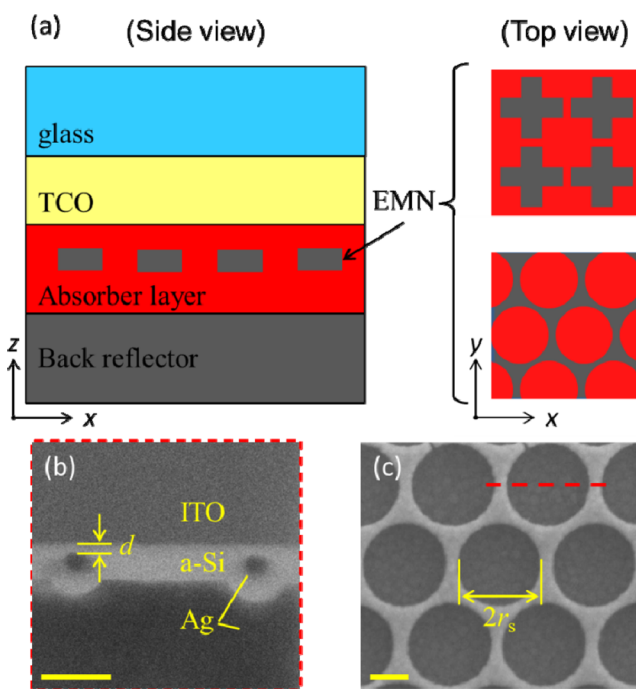


Figure 1 Design scheme (a) and SEM micrographs (b and c) of embedded metal nanopatterns (EMN). Two examples (arrays of crosses and hexagonal close-packed holes) of the EMN are shown on the right panel of (a). (b) Cross-section done by focused ion beam milling at the position indicated by the red dashed line in (c). Scale bars in (b and c), 200 nm.

3 Results and discussion

3.1 Simulated enhanced absorbance in various PV absorbers with cross-EMN

From a practical standpoint, the embedding nature of the EMN scheme is restricted to amorphous, polycrystalline, organic, and polymer ultrathin

or other non-crystalline solar cells. There are examples for the application of randomly dispersed embedded metal nanoparticles in organic solar cells [9, 10, 12, 14]. As shown in Fig. 2, we simulated the absorption within the PV layers (referring to active PV absorbers only, not including metal patterns) for one EMN scheme embedded in various amorphous PV absorbers, and compared them to situations without employing the EMN. The simulated EMN structure is a 20 nm thick Ag cross composed of two arms with 300 nm length and 100 nm width. The Ag cross-EMN is embedded in the middle of a 60 nm thick PV layer, with an embedding depth $d = 20$ nm (as defined in Fig. 1b). The PV layer is sandwiched by a 50 nm fluorine-doped tin oxide (FTO) layer and a 200 nm Ag back reflector. Optical constants of all the simulated PV absorbers are taken from the literature, including a-Si [22], a-SiGe [23], CdTe [24], $\text{CuIn}_{0.55}\text{Ga}_{0.45}\text{Se}_2$ (CIGS) [25], as well as the Ag [26] and FTO [27] layers. Note that we have calculated the absorbance in the PV layers only by calculating the ratio of the integrated power loss density within the PV layers to the total input power. Thus, the effect of any Drude losses within the metal in the optical range is taken into account [28]. These results represent the external quantum efficiencies (EQEs) of real solar cells, assuming 100% internal quantum efficiencies (IQEs), and are thus instructive for real solar cell applications.

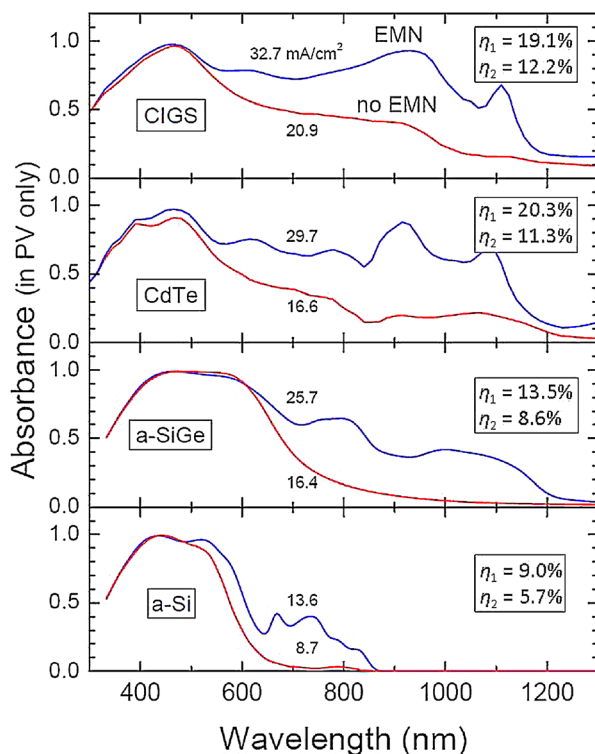


Figure 2 Simulated absorbance in various PV layers for cross-EMN design employed to various absorbers. Blue (red) line indicates absorbance in PV layer with (without) cross EMN. The calculated efficiencies with (η_1) and without (η_2) inclusion of the cross EMN are shown in boxes in the corresponding panels.

We see that without the EMN pattern, the absorbance curves strictly follow the band structure of the PV materials, tailoring off at the band edges. After the employment of the EMN, although the total volume of the PV absorber is reduced (part of it is replaced by the Ag cross-EMN), the absorbance increases over the whole spectrum, especially at regions near the band edge. After integrating the EQEs over the AM1.5 solar spectrum, we can estimate the critical current densities J_{SC} and thus the power conversion efficiencies η of the solar cells, as shown in the box for each PV absorber in Fig. 2. The calculation from J_{SC} to efficiency η is done by using typical literature values for open-circuit voltage V_{OC} and fill factor FF and using $\eta = J_{SC}V_{OC}FF/(1 \text{ kW m}^{-2})$. Our main conclusion, the fractional improvement in PV performance with EMN, however, is unaffected by choice of V_{OC} and FF. An enhancement of the efficiency for each investigated PV absorber is evident demonstrating the generality of the EMN scheme.

The collection efficiency of the photogenerated electron-hole pairs is, of course, greatly affected by their recombination rate, which partly depends on the geometrical configurations of the metal patterns. As discussed in Refs. [11, 13], a bare (uninsulated) EMN would likely increase recombination, and so be deleterious to the performance of an actual solar cell. Our simulations (not shown) suggest that this negative effect can be greatly reduced, and even eliminated, by insulating the EMN pattern with a dielectric layer as thin as 5 nm. They further show that the inclusion of this layer has only a negligible effect (of order 1%) on the optical absorbance enhancement.

3.2 Impedance analysis of the cross-EMN in CdTe absorber To deepen our understanding of this broadband enhancement effect of the EMN scheme, we carried out a theoretical impedance analysis [18] for the whole unit cell, taking the CdTe absorber layer as an example. The extraction details are described in Section 2 above. The blue (red) solid circles in Fig. 3a are simulated total absorbance of the whole CdTe cell with (without) EMN. The blue dashed line is the absorbance in CdTe layer only, the same as the curve in Fig. 2. This again shows that majority of incident light is absorbed in the CdTe layer, rather than in the metal [4]. The real and imaginary parts of the extracted impedance for the CdTe cell with and without the Ag cross-EMN are plotted in Fig. 3b and c. There are two regions where the total absorbance of the CdTe cell with EMN approach unity, at $\lambda \sim 465$ nm and ~ 915 nm, respectively (highlighted by two thick lines). At these two points, the extracted impedances of the CdTe cell with EMN match well with the free space values ($Z_{re} = 1$, $Z_{im} = 0$). On the other hand, the impedance matching condition is never satisfied for the CdTe cell without EMN. The impedance deviates from the matching condition even further at longer wavelengths toward the band gap, decreasing the performance of the solar cell. The inclusion of the EMN is thus an effective scheme for compensating for this impedance mismatch in a broadband manner. Comparing the

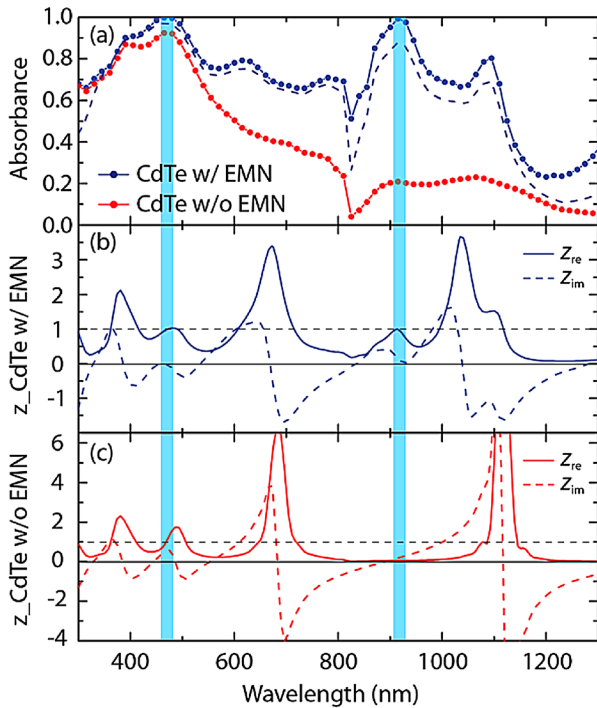


Figure 3 Extracted relative effective impedance (Z_{eff}) for the cross-EMN in CdTe absorber. (a) Total absorbance of the CdTe cell with (blue dots) and without (red dots) the inclusion of Ag cross-EMN. The blue dashed line indicates the absorbance only in the CdTe within the EMN cell structure. (b and c) Extracted real and imaginary parts of Z_{eff} for CdTe cell with (b) and without (c) cross-EMN.

solid (dashed) lines in Fig. 3b and c, we see the same overall trend, with the Z_{re} (Z_{im}) curve for the EMN case brought closer to the $Z_{\text{re}} = 1$ ($Z_{\text{im}} = 0$) line over the whole range. A detailed analysis of the broadband character of embedded (buried) metal patterns serving as an anti-reflector is recently given by Kabiri et al. [18].

The two positions where the impedance matching condition is achieved correspond to two physical modes in the CdTe cell with EMN. Profiles of the power loss density at these two wavelengths are shown in Fig. 4. The mode at ~ 465 nm is a surface plasmon (SP) mode along the top surface of the embedded Ag cross (Fig. 4c). A similar mode exists along the Ag back reflector in the CdTe cell without EMN, as shown in Fig. 4a. Thus, the total absorbance of the CdTe cells with and without EMN are both quite high at this frequency. For $\lambda \sim 915$ nm, no mode is excited for the CdTe cell without EMN, resulting in a nearly zero power loss profile, Fig. 4b. On the other hand, a gap mode is strongly excited for the EMN structure at 915 nm, as shown in Fig. 4d. This is a second order SP gap mode trapped in the region between the Ag cross and the back reflector, a phenomenon well understood as a magnetic resonance mode [29], a patch antenna mode [30], or within the framework of critical coupling [31]. This SP gap mode traps the incident photons into the CdTe in between the two Ag

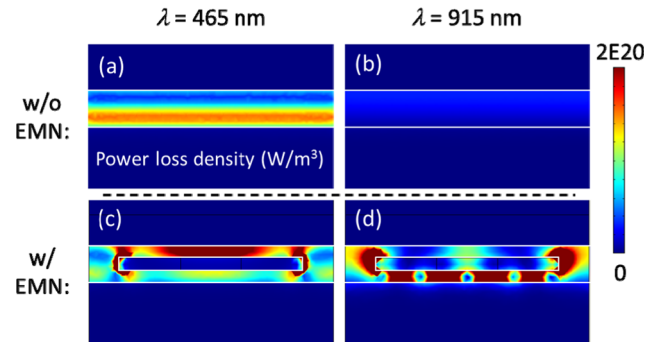


Figure 4 Profiles of the power loss density for CdTe cells with and without cross-EMN. The color bar represents 0 (blue) to $2 \times 10^{20} \text{ W m}^{-3}$ (red).

layers, without reflecting them back into free space. Thus, the absorption of CdTe mainly occurs at the gap region below the embedded Ag cross at this frequency.

3.3 Measured enhanced absorbance in a-Si with hcp-hole EMN

To experimentally verify the effectiveness of the EMN scheme, we fabricated hcp-hole EMN samples embedded in a-Si absorbers with tuned embedding depths and measured their absorbance spectra. a-Si was chosen as it is the simplest of the thin film PV material systems. The samples and measurement details are given in Section 2. The results are shown in Fig. 5. The cyan curve shows the total absorbance of the a-Si cell without hcp-hole EMN. The other curves represent the total absorbance spectra of the a-Si cell with hcp-hole EMN with increasing embedding depth from 5.3 to 18.4 nm. With increasing embedding depth, the overall total absorbance of the a-Si cell increases, as the whole a-Si cell is approaching optimum impedance matching. This is consistent with our previous results about an optimum

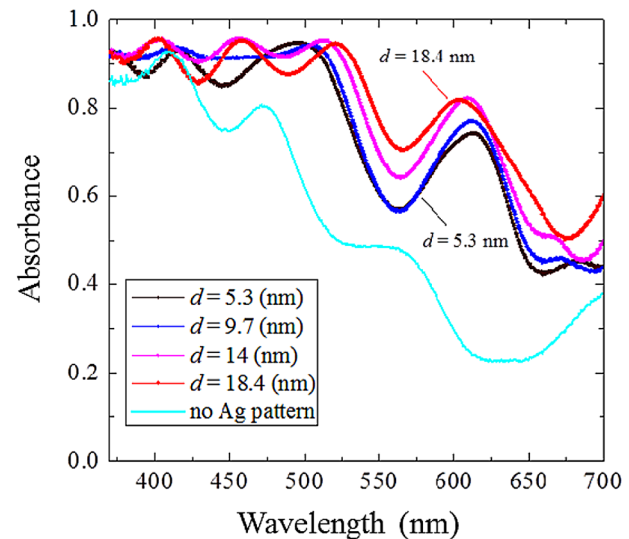


Figure 5 Measured absorbance spectra for hcp-hole EMN with tuned embedding depths.

embedding depth for EMN patterns [13]. The oscillations of the absorbance spectra around 400, 450, and 500 nm are Fabry–Perot modes formed in the 500 nm thick ITO layer. These modes will be absent in the visible range, as shown in the simulated absorbance spectra in Fig. 2, for thinner (e.g., 50 nm) ITO.

4 Conclusions We have demonstrated theoretically that an EMN scheme is a promising candidate for enhanced light absorption for a broad range of thin film solar cells, such as amorphous, polycrystalline, and organic. An impedance matching method is provided to validate the absorbance enhancement of the EMN scheme in a broad frequency range. Experimental verifications on metal nanopatterns embedded in a-Si cells are provided as a proof-of-concept of the EMN scheme. The EMN scheme may find broad applications in the solar cell industry.

Acknowledgement This work was supported by the W. M. Keck Foundation.

References

- [1] S. Pillai, K. R. Catchpole, T. Trupke, and M. A. Green, *J. Appl. Phys.* **101**, 093105 (2007).
- [2] K. R. Catchpole and A. Polman, *Opt. Express* **16**, 21793–21800 (2008).
- [3] J. N. Munday and H. A. Atwater, *Nano Lett.* **11**, 2195–2201 (2011).
- [4] Y. Wang, T. Sun, T. Paudel, Y. Zhang, Z. Ren, and K. Kempa, *Nano Lett.* **12**, 440–445 (2012).
- [5] N. Kalfagiannis, P. G. Karagiannidis, C. Pitsalidis, N. T. Panagiotopoulos, C. Gravalidis, S. Kassavetis, P. Patsalas, and S. Logothetidis, *Sol. Energy Mater. Sol. Cells* **104**, 165–174 (2012).
- [6] K. Aydin, V. E. Ferry, R. M. Briggs, and H. A. Atwater, *Nature Commun.* **2**, 517 (2011).
- [7] C. Eminiyan, F.-J. Haug, O. Cubero, X. Niquille, and C. Ballif, *Prog. Photovolt.* **19**, 260–265 (2011).
- [8] H. Tan, R. Santbergen, A. H. M. Smets, and M. Zeman, *Nano Lett.* **12**, 4070–4076 (2012).
- [9] B. P. Rand, P. Peumans, and S. R. Forrest, *J. Appl. Phys.* **96**, 7519–7526 (2004).
- [10] W. E. I. Sha, W. C. H. Choy, Y. G. Liu, and W. C. Chew, *Appl. Phys. Lett.* **99**, 113304 (2011).
- [11] F. Ye, M. J. Burns, and M. J. Naughton, *Proc. SPIE* **8111**, 811103 (2011).
- [12] C. C. D. Wang, W. C. H. Choy, C. Duan, D. D. S. Fung, W. E. I. Sha, F.-X. Xie, F. Huang, and Y. Cao, *J. Mater. Chem.* **22**, 1206–1211 (2012).
- [13] F. Ye, M. J. Burns, and M. J. Naughton, *Phys. Status Solidi A* **209**, 1829–1834 (2012).
- [14] X. Li, W. C. H. Choy, H. Lu, W. E. I. Sha, and A. H. P. Ho, *Adv. Funct. Mater.* **23**, 2728–2735 (2013).
- [15] X. Liu, T. Starr, A. F. Starr, and W. J. Padilla, *Phys. Rev. Lett.* **104**, 207403 (2010).
- [16] J. C. Hulst, D. A. Treichel, M. T. Smith, M. L. Duval, T. R. Jensen, and R. P. Van Duyne, *J. Phys. Chem. B* **103**, 3854–3863 (1999).
- [17] C. L. Haynes and R. P. Van Duyne, *J. Phys. Chem. B* **105**, 5599–5611 (2001).
- [18] A. Kabiri, E. Girgis, and F. Capasso, *Nano Lett.* **13**, 6040–6047 (2013).
- [19] D. R. Smith, S. Schultz, P. Markos, and C. M. Soukoulis, *Phys. Rev. B* **65**, 195104 (2002).
- [20] R. Liu, T. J. Cui, D. Huang, B. Zhao, and D. R. Smith, *Phys. Rev. E* **76**, 026606 (2007).
- [21] D. R. Smith, *Phys. Rev. E* **81**, 036605 (2010).
- [22] E. D. Palik (ed.), *Handbook of Optical Constants of Solids* (Academic Press, New York, 1985).
- [23] N. J. Podraza, C. R. Wronski, M. W. Horn, and R. W. Collins, *MRS Symp. Proc.* **910**, 0910-A10-01 (2006).
- [24] S. Adachi, T. Kimura, and N. Suzuki, *J. Appl. Phys.* **74**, 3435–3441 (1993).
- [25] P. D. Paulson, R. W. Birkmire, and W. N. Shafarman, *J. Appl. Phys.* **94**, 879–888 (2003).
- [26] P. B. Johnson and R. W. Christy, *Phys. Rev. B* **6**, 4370–4379 (1972).
- [27] Asahi glass; www.agc.com
- [28] M. A. Green and S. Pillai, *Nature Photon.* **6**, 130–132 (2012).
- [29] Y. Liu, S. Palomba, Y. Park, T. Zentgraf, X. Yin, and X. Zhang, *Nano Lett.* **12**, 4853–4858 (2012).
- [30] J. B. Lassiter, F. McGuire, J. J. Mock, C. Ciraci, R. T. Hill, B. J. Wiley, A. Chilkoti, and D. R. Smith, *Nano Lett.* **13**, 5866–5872 (2013).
- [31] C. Wu, B. Neuner III, and G. Shvets, *Phys. Rev. B* **84**, 075102 (2011).